An optimization algorithm for dose reduction with fluence-modulated proton CT

J. Dickmann
Department of Medical Physics, Faculty of Physics, Ludwig-Maximilians-Universität München, Am Coulombwall 1, 85748 Garching b. München, Germany

S. Rit
Univ Lyon INSA-Lyon Université Claude Bernard Lyon 1, UJM-Saint Étienne CNRS, Inserm CREATIS UMR 5220, U1206, F-69373, Lyon, France

M. Pankuch
Northwestern Medicine Chicago Proton Center, Warrenville, IL 60555, USA

R. P. Johnson
Department of Physics, University of California Santa Cruz, Santa Cruz, CA 95064, USA

R. W. Schulte
Division of Biomedical Engineering Sciences, Loma Linda University, Loma Linda, CA 92354, USA

K. Parodi and G. Dedes*
Department of Medical Physics, Faculty of Physics, Ludwig-Maximilians-Universität München, Am Coulombwall 1, 85748 Garching b. München, Germany

G. Landry[a),*]
Department of Medical Physics, Faculty of Physics, Ludwig-Maximilians-Universität München, Am Coulombwall 1, 85748 Garching b. München, Germany
Department of Radiation Oncology, University Hospital, LMU Munich, 81377, Munich, Germany
German Cancer Consortium (DKTK), 81377, Munich, Germany

(Received 23 October 2019; revised 30 January 2020; accepted for publication 5 February 2020; published 3 March 2020)

Purpose: Fluence-modulated proton computed tomography (FMpCT) using pencil beam scanning aims at achieving task-specific image noise distributions by modulating the imaging proton fluence spot-by-spot based on an object-specific noise model. In this work, we present a method for fluence field optimization and investigate its performance in dose reduction for various phantoms and image variance targets.
Methods: The proposed method uses Monte Carlo simulations of a proton CT (pCT) prototype scanner to estimate expected variance levels at uniform fluence. Using an iterative approach, we calculate a stack of target variance projections that are required to achieve the prescribed image variance, assuming a reconstruction using filtered backprojection. By fitting a pencil beam model to the ratio of uniform fluence variance and target variance, relative weights for each pencil beam can be calculated. The quality of the resulting fluence modulations is evaluated by scoring imaging doses and comparing them to those at uniform fluence, as well as evaluating conformity of the achieved variance with the prescription. For three different phantoms, we prescribed constant image variance as well as two regions-of-interest (ROI) imaging tasks with inhomogeneous image variance. The shape of the ROIs followed typical beam profiles for proton therapy.
Results: Prescription of constant image variance resulted in a dose reduction of 8.9% for a homogeneous water phantom compared to a uniform fluence scan at equal peak variance level. For a more heterogeneous head phantom, dose reduction increased to 16.0% for the same task. Prescribing two different ROIs resulted in dose reductions between 25.7% and 40.5% outside of the ROI at equal peak variance levels inside the ROI. Imaging doses inside the ROI were increased by 9.2% to 19.2% compared to the uniform fluence scan, but can be neglected assuming that the ROI agrees with the therapeutic dose region. Agreement of resulting variance maps with the prescriptions was satisfactory.
Conclusions: We developed a method for fluence field optimization based on a noise model for a real scanner used in pCT. We demonstrated that it can achieve prescribed image variance targets. A uniform fluence field was shown not to be dose optimal and dose reductions achievable with the proposed method for FMpCT were considerable, opening an interesting perspective for image guidance and adaptive therapy. © *2020 The Authors. Medical Physics published by Wiley Periodicals, Inc. on behalf of American Association of Physicists in Medicine.* [https://doi.org/10.1002/mp.14084]

Key words: dose reduction, fluence field optimization, fluence-modulated proton CT, proton CT, proton therapy

1. INTRODUCTION

Cancer treatment using intensity-modulated proton and heavier ion therapy is effective, and comes at a low risk of side-effects for the patient compared to conventional treatment modalities using x rays. The good tolerance is believed to be linked to the low dose to normal tissue when using protons for treatment.[1–4] At the same time, low-dose, frequent and accurate imaging, ideally at the treatment site, is required to ensure a safe delivery of the therapeutic doses.[5,6] Proton therapy treatment planning requires a spatial map of the relative (to water) stopping power (RSP), which in current clinical practice is acquired through a conversion from x-ray computed tomography (CT) images.[7–9] X-ray CT images are typically not acquired in treatment position and not prior to every treatment fraction, in order to keep treatment time short and imaging dose low enough that they do not compromise the dose benefit of proton therapy.[10] Direct imaging of RSP using proton computed tomography (pCT)[11–16] has been proposed to increase accuracy and to allow for a frequent, dose efficient acquisition in treatment position. Accuracies achievable with current prototypes are comparable to state-of-the art clinical dual energy x-ray CT.[7,17–19]

A further reduction of imaging dose can be achieved by modulating the imaging fluence field during the acquisition and thereby achieving a task-specific image quality. Fluence-modulated scans[20] can either aim for homogeneous variance across the whole volume, or for region-of-interest (ROI) imaging, where only the relevant part of the image is acquired at low noise and imaging dose is reduced elsewhere. Algorithms[21–24] and experimental prototypes[25–29] have been developed for fluence modulation in x-ray CT. Recently, fluence-modulated proton computed tomography (FMpCT) has also been proposed[30] and its initial experimental feasibility using pencil beam scanning was investigated.[31] The best achievable dose efficiency through fluence modulation or other techniques is a key requirement for x-ray CT[32] and most likely will be for pCT as it moves closer to the clinics. Moreover, ROI imaging is of high interest for particle therapy treatment planning and dose verification, where only a fraction of the image volume (the treatment beam path) is of relevance.[30] A challenge for FMpCT is that simple Poisson noise modeling is not sufficient, as image variance for pCT depends on the object's heterogeneity, and several contributions, including multiple Coulomb scattering, have to be taken into account for fluence-modulation.[33,34]

In this work, we present a method for fluence-field optimization in pCT using pencil beam scanning. We employ a pCT scanner-specific Monte Carlo simulation,[35] which was shown to reproduce experimental variance levels for a typical fluence field.[34] The problem of finding relative modulation factors for each pencil beam such that the summed fluence pattern results in a prescribed image variance map is a computationally expensive optimization problem which generally requires alternating between the reconstructed image domain (where the variance prescription is defined) and the projection domain (the detector data at each projection angle from which the image is reconstructed, and where the fluence modulation is defined). Therefore, we separated the problem into first solving for the projection domain variance yielding a given prescribed variance in the image domain and subsequently optimizing pencil beam weights leading to this projection domain variance. To realistically describe pencil beams in the optimization and in simulations, we established a pencil beam model based on experimental data. In a simulation study, we estimated dose savings for FMpCT using three different phantoms, and compared our proposed solution with a straightforward intersection-based fluence modulation.[31] We also verified that the resulting variance map approaches the target variance. Both a constant variance target as well as two ROIs following typical treatment beam paths were investigated.

2. MATERIALS AND METHODS

2.A. Simulation framework

The Monte Carlo simulation framework[35] used in this study is a detailed model of the phase II pCT prototype scanner.[13] It is based on the GEANT4 toolkit[36] version 10.2.p01. Details about the modeling of physics processes can be found in literature, where the platform was validated for its fidelity in terms of RSP.[19,35] A previous study[34] improved the platform for reproducing variance levels of experimental scans. With respect to that work, the beam model was modified, and is described below. Imaging doses, in the form of absorbed physical dose, were scored on a centered grid of 125 × 125 × 35 voxels with a uniform voxel size of 2 mm and summed for all projection angles.

The simulation framework outputs data in the same format as the prototype scanner. It records position and direction information of individual protons before and after the object, as well as the proton's residual energy. Using a calibration,[37] the residual energy can be mapped to a water-equivalent path length (WEPL), which is the line integral over the RSP of the object along the curved path of the proton. Because measurements are available for every detected proton, these data are referred to as "list-mode."

2.B. Image reconstruction

To reconstruct RSP images from the list-mode data, a most likely path[38] is estimated for every proton from the tracking information. The path information is taken into account by performing distance-driven binning and applying a special cone-beam filtered backprojection algorithm.[39] In total, 90 projections from rotation angles covering a full rotation were used. This relatively low number of projections was chosen to satisfy experimental timing constraints and to allow for a future experimental validation of this work. Reconstructions were performed on a grid of 250 × 250 × 70 voxels with a uniform size of 1 mm. For performing data cuts,[12,38,39] the grid was 125 × 125 pixels with a uniform size of 2 mm.

Binning of data into distance-driven projections was performed on a grid of 250 × 250 × 70 voxels with a uniform size of 1 mm. All grids were centered on the isocenter.

Assume a voxel centered in (u,v,d) in the three-dimensional (3D) distance-driven projection, where d is the binning depth and u and v are the coordinates normal to it. We can identify a set of protons such that the most likely path of every proton crosses the voxel volume around (u,v,d). The number of protons in that set is then referred to as the "counts" $C(u,v,d)$. These counts only consider protons used for image reconstruction and therefore are reduced compared to the incident protons due to interactions with the object and cuts on the data. In contrast to that, counts in the absence of interactions and cuts are referred to as $F(u,v,d)$ throughout the paper. The point $u = v = d = 0$ is the location of the isocenter, where the rotation axis is located.

2.C. Phantoms

In the simulation study, three different phantoms with a physical counterpart were used. The water phantom is a cylindrical container made from polystyrene (outer diameter 150.5 mm, wall thickness 6.35 mm) and filled with distilled water. The CTP404 phantom (*Phantom Laboratory*, New York, USA) is a commercial sensitometric phantom with a cylindrical shape (diameter 150) and several tissue-equivalent inserts and two cylinders filled with air. Both phantoms were implemented in the simulation as analytical models. The pediatric head phantom (ATOM®, Model 715 HN, *CIRS Inc*., Norfolk, USA) models the anatomy of a 5-yr-old child and was implemented as a voxelized phantom in the simulation.[40] Previous publications[34,35,40] can be consulted for details about the phantoms.

2.D. Gaussian pencil beam model

To allow for the flexible simulation of FMpCT data, an analytical pencil beam model was derived from experimental tracking data acquired at the pencil beam scanning beamline of the Northwestern Medicine Chicago Proton Center without phantom. Using the timing information of the scanner, a count rate was calculated in steps of 0.8 ms, allowing for the separation of individual pencil beams as the count rate dropped in between two spots. The separated data were processed individually by estimating most likely paths and performing distance-driven binning.[39]

For each pencil beam b, this resulted in a 3D experimental counts map $C_b(u,v,d)$. We fitted the Gaussian model

$$G(u,v,d) = \frac{N_0}{2\pi\sigma_u'\sigma_v'} \cdot \exp\left(-\frac{(u-u_0'(d))^2}{2\sigma_u'^2} - \frac{(v-v_0'(d))^2}{2\sigma_v'^2}\right) \tag{1}$$

to each pencil beam's C_b, where N_0 is the total number of protons per pencil beam, and $(u_0'(d), v_0'(d))$ is the pencil beam center at depth d. The pencil beam center is assumed to diverge linearly with the binning depth, such that $u_0'(d) = u_0 \cdot (1 + \delta_u \cdot d)$ and $v_0'(d)$ analogously, where (u_0, v_0) is the pencil beam center at $d = 0$ and δ_u and δ_v are the linear divergence factors. By construction, the isocenter-beam for $u_0 = v_0 = 0$ is parallel to the d-axis. The $\sigma_u' = \sigma_u \cdot \sqrt{1 + \delta_u^2 u_0^2}$ and σ_v' analogously are the beam widths projected to a plane normal to the d-axis while σ_u and σ_v are the actual beam widths. This resulted in a fit with seven open parameters (N_0, u_0, v_0, σ_u, σ_v, δ_u, δ_v), which was performed for each individual pencil beam by minimization of the squared deviation. The parameters σ_u, σ_v, δ_u and δ_v were not specific to one pencil beam, and estimates for them were therefore found as the mean value over all pencil beams. N_0, v_0 and u_0 were open parameters specific to a given pencil beam, but overwritten in subsequent simulations of different pencil beam patterns. They are therefore not reported.

2.D.1. Simulation of pencil beams

All datasets were generated by shooting a regular grid of simulated proton pencil beams. At $d = 0$, neighboring pencil beams were interspaced by $\Delta_{PB,u} = 12$ mm along u and $\Delta_{PB,v} = 8$ mm along v. The pencil beam grid was offset in u by $\Delta_{PB,u}/4 = 3$ mm so that the summed fluence from two opposing angles was homogeneous. This helped to reduce the total number of pencil beams and thereby reduce the complexity of the optimization. In the simulation platform, protons were emitted from a point $(u_0 \cdot (1 + \delta_u \cdot d_0), v_0 \cdot (1 + \delta_v \cdot d_0), d_0) + (r_u, r_v, 0)$, where $d_0 = -400$ mm and r_u and r_v are normally distributed random numbers with a standard deviation of σ_u and σ_v, respectively. The point d_0 is just before the front tracker and was chosen in agreement to previous investigations.[34] Protons were assumed to have an initial direction vector of $(u_0\delta_u, v_0\delta_v, 1)$. The beam centers (u_0, v_0) were chosen according to the pencil beam grid defined above. For nonmodulated scans, N_0 was set to a default value $N_0 = N$ for all pencil beams. For modulated scans, it was $N_0 = m_b^\alpha N$ for a pencil beam modulated with a factor m_b^α. The proton's initial energy was set to 200.00 ± 0.66 MeV, which is the standard mean energy used experimentally. The energy spread was determined in a previous study[34] and agrees with experimental data acquired at the beamline at the Northwestern Medicine Chicago Proton Center, albeit with a wider spot size setting.

2.D.2. Pencil beam reference counts

To optimize pencil beam weights, a reference of the proton counts for every pencil beam is needed. This reference serves as a basis function for the fluence modulation and should not take into account interactions with the object. It can be generated for every pencil beam b using the Gaussian model

$$F_b(u,v,d) = G(u,v,d)|_{N_0=N, u_0=u_b, v_0=v_b} \tag{2}$$

assuming a pencil beam center (u_b, v_b) according to the regular grid and a constant number of protons N which is equal for all pencil beams.

2.D.3. Optimization of pencil beam weights

Using the F_b as basis functions, it is possible to generate an arbitrary counts field C^α for rotation angle α by finding weights w_b^α, such that C^α is expressed as a linear combination of the reference counts F_b from Eq. (2). Weights were found by minimizing the squared deviation, and therefore

$$w_b^\alpha(C^\alpha) = \arg\min_{w_b^\alpha} \iint \mathrm{d}u\mathrm{d}v \left(C^\alpha(u,v,0) - \sum_b w_b^\alpha F_b(u,v,0) \right)^2. \tag{3}$$

Integration was performed over u and v, but only the isocenter binning depth $d = 0$ was considered. Optimization was performed using the method of Nelder and Mead.[41]

2.E. Proposed algorithm for fluence field optimization

Fluence field optimization requires finding a set of fluence modulation factors $m_b^\alpha \in [0,1]$ for pencil beam b at rotation angle α, such that the resulting pCT reconstruction best achieves a given image variance target $V_{\text{target}}(x,y,z)$. The proposed method for fluence field optimization is performed in the projection domain (denoted by coordinates (u,v,d) and the rotation angle α) instead of the image domain (denoted by coordinates (x,y,z)). The method is sketched in Fig. 1 and consists of the following three steps, which will be detailed in Sections 2.E.1–2.E.3:

1. For a given phantom, find the resulting variance $V_{\text{unit}}^\alpha(u,v,d)$ in the projection domain for a unit fluence simulation with $m_b^\alpha = 1$ for all pencil beams.
2. For a given image variance target $V_{\text{target}}(x,y,z)$, find a stack of variance levels in the projection domain $V_{\text{target}}^\alpha(u,v,d)$ that yields the image variance target.
3. Calculate the pixel-wise counts target $C_{\text{target}}^\alpha(u,v,d)$. Then, optimize weights that yield the counts target according to Eq. (3).

The algorithm extends ideas from literature for x-ray CT[21,22] to requirements of pCT such as the 3D projections due to distance-driven binning[39] and a more complex noise model.[33,34] It is, to our knowledge, not equivalent to any existing approach as it is performed in projection domain and computationally feasible without simplification to a parallel-beam geometry.

2.E.1. Step 1: variance at unit fluence prediction

To find variance levels at unit fluence for a given phantom, we employed a Monte Carlo simulation using the beam model described in Section 2.D and $m_b^\alpha = 1$ for all pencil beams and rotation angles. This step requires an object model according to Section 2.C and resulted in counts $C_{\text{unit}}^\alpha(u,v,d)$, which were reduced compared to the reference counts $F_{\text{unit}}(u,v,d) = \sum_b F_b(u,v,d)$ due to interactions with the object. For every point (u,v,d) in the projection, a set of $n = C_{\text{unit}}^\alpha(u,v,d)$ WEPLs, $\{p\}$, was found such that the voxel around (u,v,d) was crossed by the most likely path of each of the selected protons.[39] The unit fluence variance was then the squared error of the mean

$$V_{\text{unit}}^\alpha(u,v,d) = \mathrm{Var}[\{p\}]/C_{\text{unit}}^\alpha(u,v,d). \tag{4}$$

Given a variance projection stack $V_{\text{unit}}^\alpha(u,v,d)$, the corresponding image variance $V_{\text{unit}}(x,y,z)$ can be calculated analytically as reconstruction was performed using filtered backprojection. Please refer to previous publications[33,34] for details about variance calculations for pCT and for variance reconstruction in general.[42]

2.E.2. Step 2: iterative variance forward projection

Finding a stack of variance projections $V_{\text{target}}^\alpha(u,v,d)$ whose variance reconstruction[33] yields a given image variance target $V_{\text{target}}(x,y,z)$ is a problem with a large set of solutions. We therefore aimed to find the inverse operation of variance reconstruction,[42] that is, a "variance forward projection." An initial guess $V_0^\alpha(u,v,d)$ could be obtained by performing ray tracing[43] through the image variance target $V_{\text{target}}(x,y,z)$ followed by ramp filtration. The additional filtration was motivated by the fact that variance reconstruction is very close to a simple unfiltered backprojection.[42] Since ray-tracing is the inverse operation to filtered backprojection, an additional ramp-filtration was required. While such forward- and backprojection yield V_{target} again, this often yields unphysical negative variance projection values and amplifies noise. Therefore, a median filter was applied to the ramp-filtered projections followed by thresholding to positive values.

To minimize the error introduced by thresholding, we employed an iterative approach by applying variance reconstruction to the i-th set of variance projections $V_i^\alpha(u,v,d)$ yielding a variance volume $V_i(x,y,z)$. Again, using ray-tracing, the difference volume $V_{\text{target}}(x,y,z) - V_i(x,y,z)$ was forward-projected and added to the current stack of variance projections. In every iteration, the variance projection values were forced to be positive. This will converge to a set of physical (i.e., strictly positive) variance projections that yield an image variance approaching $V_{\text{target}}(x,y,z)$.

2.E.3. Step 3: fluence optimization

By definition, the variance projection values in Eq. (4) are inversely proportional to the number of contributing protons C. Therefore, the pixel-wise counts required to achieve the variance target could be calculated as $(V_{\text{unit}}^\alpha/V_{\text{target}}^\alpha) \cdot C_{\text{unit}}^\alpha$. However, for low counts, we need to consider that C follows a Poisson distribution (contrary to a normal distribution at sufficiently high counts) and therefore an additional correction function

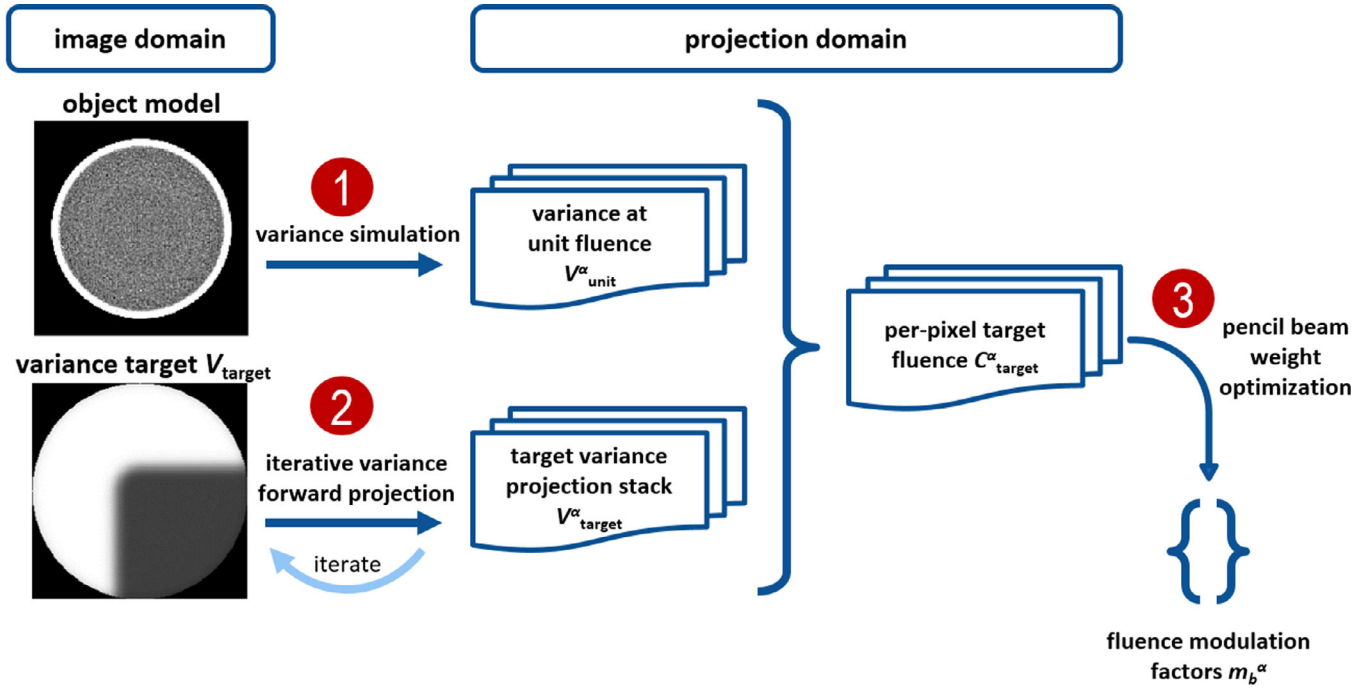

FIG. 1. Workflow for optimization of fluence modulation factors m_b^{α}, given an object model and a variance target V_{target}. [Color figure can be viewed at wileyonlinelibrary.com]

$$k(C) = C \cdot \sum_{n'=1}^{\infty} P_C(n') \cdot \beta_{n',C} = C^2 \sum_{n'=1}^{\infty} \frac{P_C(n')}{n'} \tag{5}$$

needs to be introduced, where $P_C(n') = C^{n'} \exp(-C)/n'!$ is the Poisson probability of detecting n' protons instead of the expectation value of C and $\beta_{n',C} = C/n'$ is the relative change in variance if n' instead of C protons were detected. The function $k(C)$ was stored in a lookup table for all relevant integer values of C up to 300 by numerically calculating the infinite sum for 1000 summands. Since $\lim_{C\mapsto\infty} k(C)/C = 1$ and $k(300)/300 = 1.0033$ we assumed $k(C) = C$ for all $C > 300$. Furthermore, $k(C)$ was thresholded to return at least $C_{\min} = 8$ protons to avoid detector elements with missing information.

We used an optimization according to Eq. (3) to find pencil beam weights $w_b^{\alpha}(C^{\alpha}_{\text{target}})$ which achieve the pixel-wise projection counts target of

$$C^{\alpha}_{\text{target}}(u,v,d) = k\left[\frac{V^{\alpha}_{\text{unit}}(u,v,d)}{V^{\alpha}_{\text{target}}(u,v,d)} \cdot C^{\alpha}_{\text{unit}}(u,v,d)\right]. \tag{6}$$

Due to the fact that C^{α}_{unit} and $C^{\alpha}_{\text{target}}$ are both affected by interactions with the object, the optimization also needed to be performed for unit fluence allowing for an elimination of the effect of attenuation and scattering. This resulted in fluence modulation factors

$$m_b^{\alpha} = \frac{w_b^{\alpha}(C^{\alpha}_{\text{target}})}{w_b^{\alpha}(C^{\alpha}_{\text{unit}})} \tag{7}$$

with numerator and denominator as defined in Eq. (3). Due to the normalization, these factors were corrected for interactions with the object and thus could be used to simulate an FMpCT scan according to Section 2.D.1.

2.E.4. Reference approach

A simpler approach to fluence field optimization, which was used in previous works,[31] is to perform a binary modulation with two fluence levels. In image domain, a ROI is defined as a set of voxels that should be imaged with high fluence. A pencil beam is assigned a high imaging fluence if its central axis intersects the ROI, and a low imaging fluence otherwise. The fluence modulation factors were

$$m_b^{\alpha} = \begin{cases} 1 & \text{if intersecting} \\ \gamma & \text{otherwise} \end{cases}, \tag{8}$$

where $0 < \gamma < 1$ is the modulation strength, which was chosen to be equal to the contrast of the variance prescription of the proposed method.

2.F. Simulation study

In a simulation study, we prescribed three different image variance targets, which can be appreciated in Fig. 2: (a) constant variance V_{ROI} throughout the imaged object; (b) FMpCT prescription A (variance V_{ROI} inside one quadrant of the imaged object and $4 \cdot V_{\text{ROI}}$ elsewhere); and (c) FMpCT prescription B (V_{ROI} inside a central rectangular region and $4 \cdot V_{\text{ROI}}$ elsewhere). Variance targets are used in step b of the proposed algorithm, and therefore independent of the imaged object. In agreement to previous investigations[31], the prescription contrast of 4 was chosen such that it is higher than the variance dynamic range of a unit fluence scan,[34] but

reasonably achievable without expecting regions with vanishing counts or distortions of RSP accuracy.

Previous investigations[34] have shown that a uniform fluence does not yield a constant variance for pCT. Therefore, the constant variance prescription is the most dose-efficient image, if the complete image is required for diagnosis. Prescriptions A and B model two treatment scenarios, where the treatment beam path is coming from 90° and 180° in A and from 90° and 270° in B. Prescriptions were slightly blurred as sharp gradients in image variance cannot be achieved due to the ramp filtration involved in reconstruction. Throughout this work, we use the nomenclature "constant," "A" and "B" to refer to the three prescriptions.

For all phantoms, we first simulated a high dose unit fluence dataset with $m_i^z = 1$. The mean incident proton fluence was chosen to be $133\,\mathrm{mm}^{-2}$ such that it yielded a typical imaging dose for pCT of about 1.4 mGy,[12] when summed over all projections. We then chose the value of V_{ROI} for each phantom as the 95th percentile value of the variance in the unit fluence scan. For the water phantom, this was $V_{\mathrm{ROI}} = 4.61 \times 10^{-4}$, for the CTP404 phantom $V_{\mathrm{ROI}} = 5.89 \times 10^{-4}$, and for the head phantom $V_{\mathrm{ROI}} = 11.96 \times 10^{-4}$. These values are consistent with previous studies.[34]

For the CTP404 phantom, RSP values of the phantom body and of two inserts inside the ROI were evaluated and compared to the unit fluence scenario. The body consisted of epoxy (RSP = 1.144), and inserts were made from Teflon (RSP = 1.791) and polymethylpentene (RSP = 0.883). RSP values were calculated with GEANT4 at a proton energy of 150 MeV and agreed with previous experiments.[35]

For a fair comparison of imaging doses, we computed the 95th percentile variance value v_{95}^{ROI} inside the ROI (inside the whole phantom for unit fluence) and calculated a linear correction factor $\eta = v_{95}^{\mathrm{ROI}}/V_{\mathrm{ROI}}$. Doses and counts were multiplied by η, variances were multiplied by $1/\eta$. The choice of the 95th percentile value over the mean or the maximum value is a compromise between the requirement that variances should be at V_{ROI} or lower, and tolerating outliers. As the water and the CTP404 phantom were thin, the percentile value was calculated only within the displayed central slice. For the head phantom, which covered the entire height of the detector aperture, it was calculated over the full volume. To avoid the variance evaluation being dominated by increased noise at the hull of the phantom as discussed in previous works,[33,34] we determined the shape of the hull by setting an RSP threshold of 0.5 and eroding the hull by 7 mm. Values outside this region were disregarded. The ROI region and the out-of-ROI region are indicated in Fig. 2 for fluence modulations A and B.

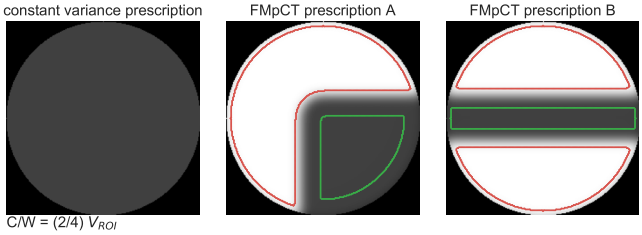

FIG. 2. Three different image variance targets for the simulation study. The region-of-interest (ROI) region and the out-of-ROI region are indicated in green and red respectively. The display center (C) and window (W) is noted below the figure. [Color figure can be viewed at wileyonlinelibrary.com]

3. RESULTS

3.A. Gaussian pencil beam model

In an experimental dataset without phantom, we determined the beam spreads of the Gaussian beam model to be $\sigma_u = (4.04 \pm 0.08)$ mm and $\sigma_v = (5.24 \pm 0.09)$ mm. The divergence was $\delta_u = (5.2 \pm 0.6) \times 10^{-4}\,\mathrm{mm}^{-1}$ and $\delta_u = (5.8 \pm 1.4) \times 10^{-4}\mathrm{mm}^{-1}$. The beam spread in the u direction was significantly smaller compared to the beam spread in v direction. Divergence in the u and v direction did not differ outside of the uncertainty bounds. The distances from the isocenter to a virtual source were $1/\delta_u = (1.9 \pm 0.2)$ m and $1/\delta_v = (1.7 \pm 0.4)$ m, which agrees with the position of the scanning magnets, which is 1.8 m from the isocenter. The stated parameters were used in all the following evaluations.

3.B. Variance optimization

3.B.1. Iterative variance forward projection

For step 2 of the proposed method, Fig. 3(a) shows error measures as a function of the iteration number. The root-mean-square (RMS) error as well as the mean error between the current variance volume $V_i(x, y, z)$ and the variance target $V_{\mathrm{target}}(x, y, z)$ are calculated within the field-of-view. The fastest convergence is observed for the constant variance prescription, while both FMpCT prescriptions A and B show a remaining RMS error that only reduces slowly in every iteration. The mean error quickly drops to zero within the first iterations. The relative change in RMS error for all prescriptions was below 1% per iteration when they were stopped. Figures 3(b) to 3(d) show $V_i(x, y, z)$ for prescription B at three different iterations. At iteration 20, the high-variance region has reached the correct value, while in the low-variance region artifacts remain, but decrease up to the last iteration.

3.B.2. Fluence optimization

To validate the use of the correction function $k(C)$, Fig. 4 shows $k(C)/C$ together with the relative increase in the image variance V_C at mean counts C. The relative increase is calculated as $(V_C \cdot C)/(V_{C_\infty} \cdot C_\infty)$ for $C_\infty = 310$ for simulated pCT data. Both curves agree, which shows that variance increases overproportionally for low counts and that the correction function $k(C)$ describes this well.

Figure 5 shows intermediate steps of the fluence optimization for the pediatric head phantom and variance prescription

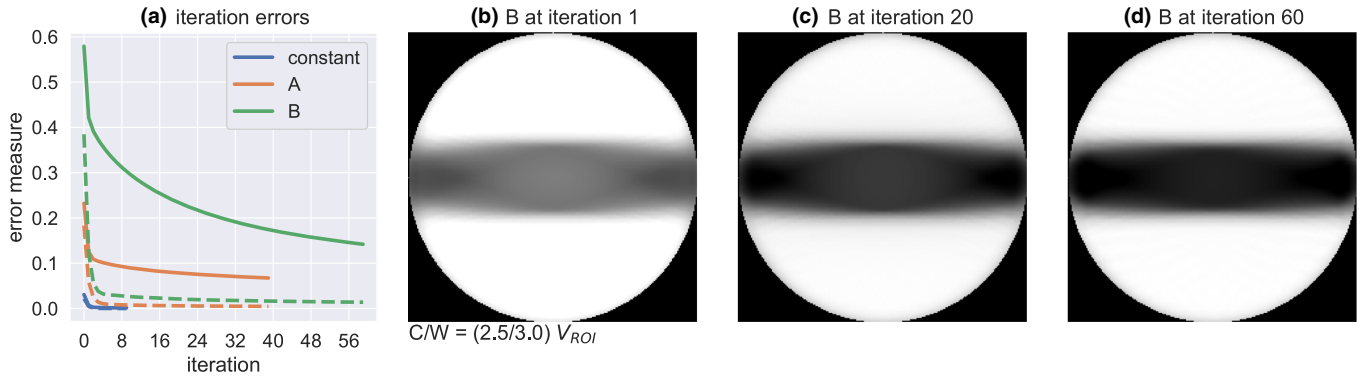

FIG. 3. (a) Root-mean-square error (solid) and mean error (dashed) as a function of the iteration number of the three image variance targets. (b)–(d) Reconstructed variance volumes for prescription B for different iterations. The display center (C) and window (W) is noted below the figure. [Color figure can be viewed at wileyonlinelibrary.com]

A. All projection data are shown as sinograms plotted as a function of the detector position in u direction and the rotation angle. Only data for $v = d = 0$ are shown. In Fig. 5(a), variance at unit fluence $V^{\alpha}_{\text{unit}}(u,0,0)$ is shown (step 1 of the algorithm), which is high at the periphery of the object and around heterogeneities, as discussed in previous works.[34] Figure 5(b) shows the variance target $V^{\alpha}_{\text{target}}(u,0,0)$ as a result of the iterative optimization (step 2). Figure 5(c) shows the pixel-wise counts target for fluence modulation $C^{\alpha}_{\text{target}}(u,0,0)$ (step3) as given by Eq. (6). Parts of the variance target in (b) are assigned a value of 0, and receive the unit fluence in (c). In Fig. 5(d), the counts target is fitted by the pencil beam model to get the weights required for fluence modulation (also step 3). This can be calculated as $\sum_b w^{\alpha}_b F_b(u,v,d)$. Some small features of (c) are not present in (d) if they are smaller than the extension of a pencil beam.

3.C. Simulation study

Figures 6 and 7 show simulated fluence modulations for all phantoms. RSP, variance, and dose maps are shown together with the counts sinograms. For the water phantom imaged with unit fluence [Fig. 6(a)], counts, and dose were homogeneous throughout the phantom, variance was reduced in the center. This reduction was compensated in Fig. 6(b) for the constant variance target, where instead counts and imaging dose were reduced in the center and variance was homogeneous across the phantom, except for a steep increase in the hull. The fluence modulations in Figs. 6(c) and 6(e) for variance targets A and B can already be appreciated in the RSP maps. Variance levels followed the prescription with a sharp gradient. For prescription A some streaks of high variance were observed within the ROI. Using the reference approach in Figs. 6(d) and 6(f), conformity of variance and dose maps with the ROI was degraded, in particular for prescription B, where variance and dose are at the same level as in the unit fluence scan for most of the phantom and the change in variance cannot be seen in the RSP maps. In the counts sinograms, regions of increased counts roughly agreed with those using the optimization, but were uniform, as required. Instead, using the optimization, a heterogeneous counts pattern was observed.

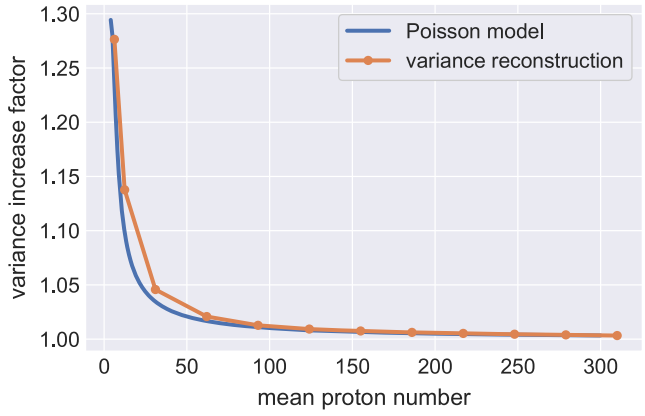

FIG. 4. Overproportional increase of image variance with decreasing counts in a simulation with varying mean proton number C and agreement with the fluence correction function $k(C)/C$. [Color figure can be viewed at wileyonlinelibrary.com]

For the CTP404 phantom [Figs. 7(a) and 7(b)] and the head phantom [Figs. 7(c) and 7(d)], the variance increased around heterogeneities both in unit fluence and fluence-modulated scans. For the head phantom in particular, the palate exhibited locally elevated variance levels. The fluence modulation with prescription A was less conformal, compared to those of the water phantom. In particular for the CTP404 phantom, the variance contrast was impaired. Counts sinograms for prescription A in Figs. 6(c) and 7(b) and 7(d) are similar, but phantom-specific differences are noticeable.

Mean imaging doses are summarized in Fig. 8, where the fluence modulation, the mean dose over the whole phantom as well as the mean doses in the ROI region and the out-of-ROI region are reported. For the water phantom, prescribing constant variance resulted in a dose reduction of 8.9% compared to the unit fluence dose. For the ROI fluence modulations, dose saving outside the ROI was 40.5% for prescription A and 25.7% for prescription B. Using the simple reference approach, dose reductions were less pronounced and dropped to 29.2% and 13.2% respectively. For the FMpCT prescription A and the CTP404 phantom as well as

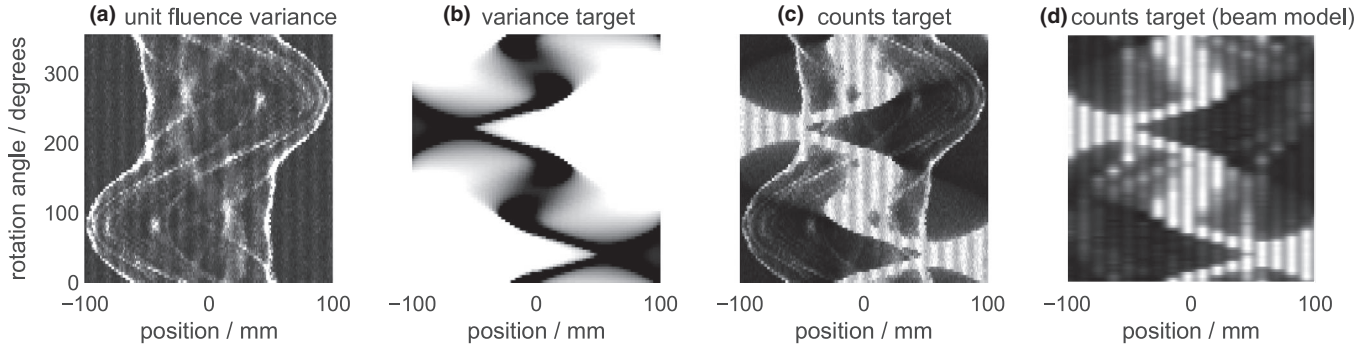

FIG. 5. Intermediate results of the fluence optimization process for the pediatric head phantom and the orthogonal beams variance target: (a) unit fluence variance $V^{\alpha}_{\text{unit}}(u,0,0)$, (b) variance target $V^{\alpha}_{\text{target}}(u,0,0)$, (c) pixel-wise target counts $C^{\alpha}_{\text{target}}(u,0,0)$, and (d) target counts as fitted by the beam model. Data are shown as a function of the rotation angle α and the detector coordinate u. For display a center of 0.4 mm^2 and a window of 0.8 mm^2 has been applied for variances, and a center of 80 and a window of 160 for counts.

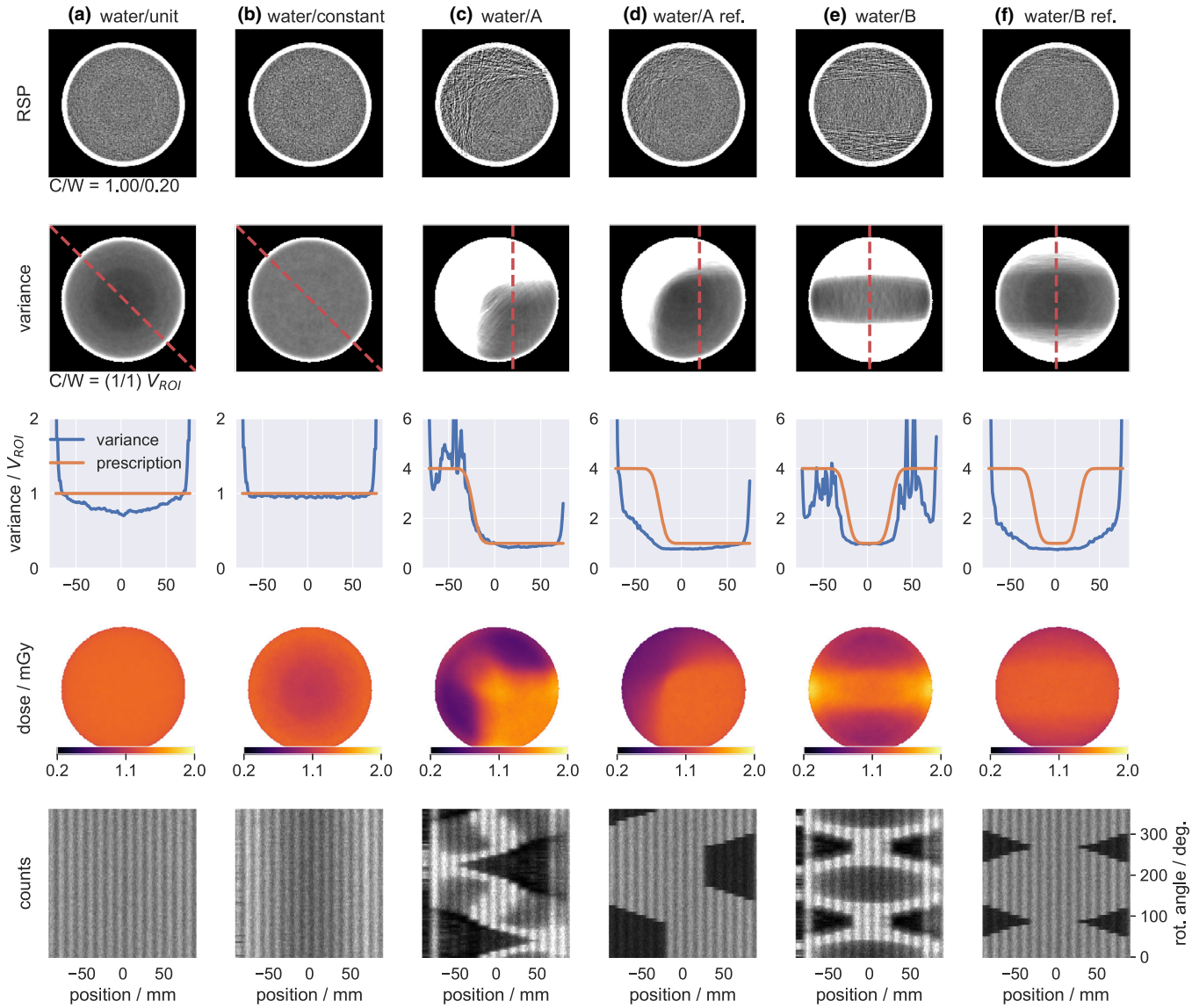

FIG. 6. Simulation study for the water phantom and variance targets as indicated in the titles. Sinograms are shown for $v = d = 0$. Center (C) and window (W) settings for display of RSP and variance values are given. [Color figure can be viewed at wileyonlinelibrary.com]

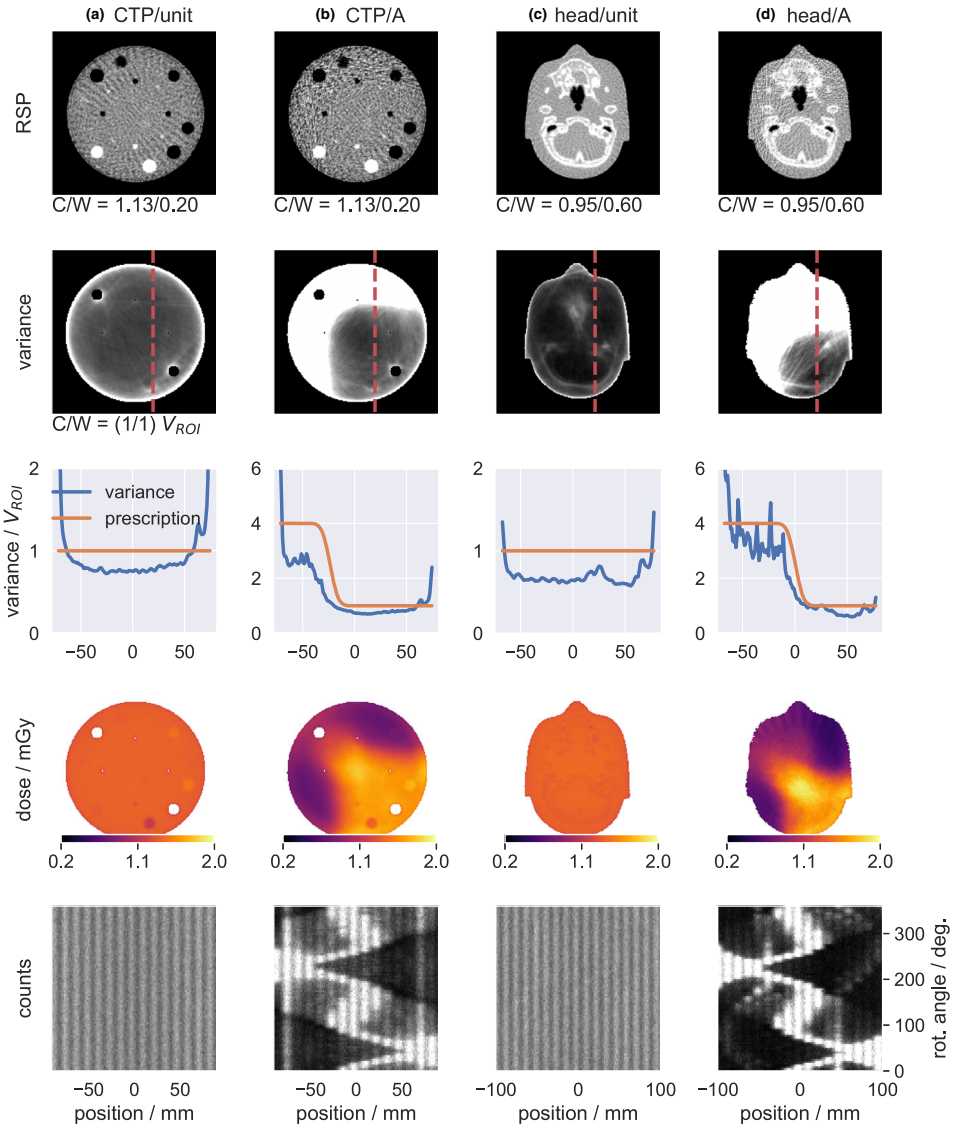

FIG. 7. Simulation study for the CTP404 and the head phantom, and variance targets as indicated in the titles. Sinograms are shown for $v = d = 0$. Center (C) and window (W) settings for display of RSP and variance values are given. [Color figure can be viewed at wileyonlinelibrary.com]

the head phantom, dose savings outside the ROI were slightly lower compared to the 40.5% of the water phantom (35.4% and 38.9% respectively). For all phantoms, fluence modulations A and B achieved a lower dose outside the ROI compared to the unit fluence, but after normalization with η required a higher dose inside the ROI by 9.2% to 19.2%. Doses inside the ROI were approximately constant for the reference approach. Mean doses over the whole phantom were reduced by 7.2% to 13.1% using the reference approach and by 9.8% to 18.6% for the FMpCT optimizations.

For the CTP404 phantom, the two inserts and the body inside the ROI had an RSP value of 1.776, 0.881, and 1.143, compared to 1.776, 0.879, and 1.143 for the unit fluence case.

Figure 9 shows the head phantom with unit fluence (a,b) and for the constant variance target (c,d) both in a sagittal view (a,c) and a coronal view (b,d). Dose is homogeneous for the unit fluence imaging, but the variance is notably lower in the back of the head and around the spinal cord compared to regions around the palate and the nasal cavities. These variations were compensated for in the fluence modulations achieving more homogeneous variance levels at reduced doses in regions where variance was low for unit fluence. Mean dose over the whole phantom was 1.15 mGy compared to 1.37 mGy in the unit fluence case (16.0% reduction). Around the palate and the nasal cavities, dose is increased in the fluence-modulated scan, which is not expected and may be due to the normalization by η.

4. DISCUSSION

4.A. Gaussian pencil beam model

We found parameters of a Gaussian pencil beam model that allowed us to describe pencil beams at arbitrary fluences and

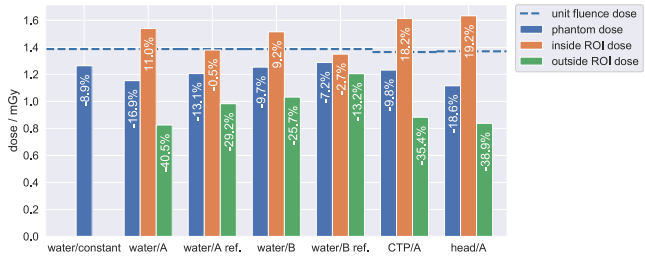

FIG. 8. Mean imaging doses for the simulation study. The dashed line indicates the unit fluence dose while bars show the average phantom dose and doses inside and outside the region-of-interest. The relative dose change compared to unit fluence dose is given inside the bars. Unit fluences were equal for all phantoms, but unit fluence doses differed slightly. [Color figure can be viewed at wileyonlinelibrary.com]

positions. This is a key component of the fluence modulation scheme, as it allows us to find a linear combination of a regular grid of pencil beams that achieves the required counts as calculated by our algorithm. Uncertainty bounds for fits in v direction were consistently larger than those in u direction, in particular for the divergence parameter δ. This was because the detector aperture is smaller in u direction and less datapoints were available. The beam spread σ_v was significantly larger than σ_u. While this anisotropy is not expected for clinical operation, it may have been caused by operating the beam line in research mode and modifying beam optics settings to keep proton fluence low and viable for the scanner. For future experimental studies, certain model parameters, such as the beam energy spread, may require adjustment to exactly match experimental variance levels.

4.B. Variance optimization

4.B.1. Iterative variance forward projection

Using an iterative approach, we calculated stacks of variance projections that yield a desired variance map in image space. Depending on the complexity of the variance prescription, this required a different amount of iterations and a nonzero RMS error remained. The easiest case (constant variance target), did not require negative variance values (a constant stack of variance projections would yield a constant image variance) and therefore converged quickly. The two inhomogeneous variance targets A and B did suffer from the positivity requirement and therefore only slowly converged toward a reduced RMS error. While with negative variance values, a (close to) zero RMS error would be possible, this was not the case when requiring physical variance values. The variance target stacks therefore already contained an inherent error, which impacted the achievable variance contrast. However, it did not impact fluence modulation in general, as the prescribed fluences could be rescaled, such that V_{ROI} was achieved inside the ROI.

4.B.2. Fluence optimization

We calculated the counts target according to Eq. (6), which could run into a lower and an upper limit. Firstly, to ensure that that data were available throughout the projection, we required at least C_{min} protons in every pixel. Secondly, to avoid unreasonably high imaging doses, only fluence modulation factors $m_b^{\alpha} \leq 1$ were allowed, even if the variance target from the previous step (iterative variance forward projection) was zero. This was relevant, in particular, to the hull of the object, which is also a limited area to be traversed by a therapeutic proton beam. Again, both limits impacted achievable variance contrast, but V_{ROI} could be achieved in the ROI by rescaling with η. Due to the limitation of pencil beams with a finite size, small variance features were averaged out, which may impact homogeneity of the achieved variance, in particular for phantoms with strong heterogeneities.

4.C. Simulation study

We simulated FMpCT scans for different phantoms and variance targets demonstrating two possible applications for dose reduction using fluence modulation: (a) for achieving constant variance throughout the object and (b) concentrating imaging dose in a high image quality ROI and reducing it elsewhere.

The dose reduction for constant variance with the homogeneous water phantom was 8.9%, which already is considerable. As shown in previous investigations,[34] variance for

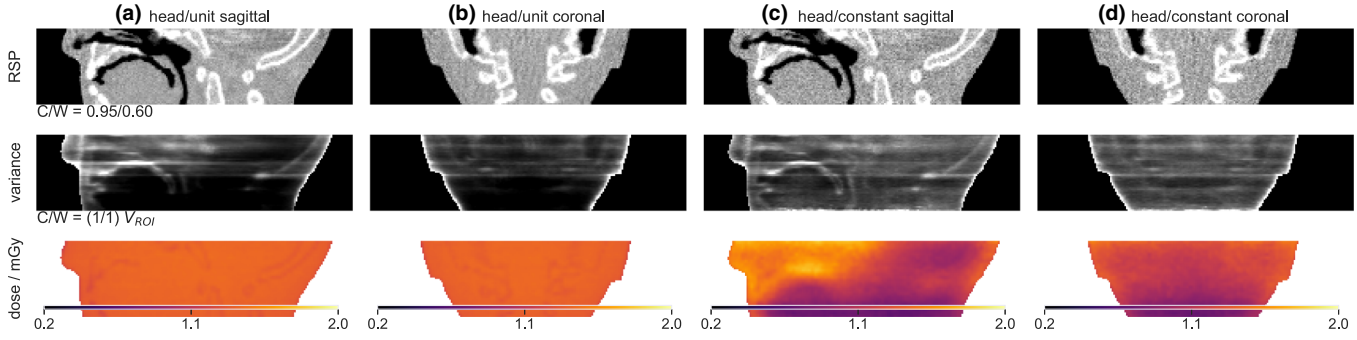

FIG. 9. Simulation study for the pediatric head phantom with unit fluence (a), (b) and the constant variance target (c), (d). Row by row, the RSP, variance, and imaging dose are shown. Sagittal and coronal views are shown. Center (C) and window (W) settings for display of RSP and variance values are given. [Color figure can be viewed at wileyonlinelibrary.com]

heterogeneous phantoms is dominated by multiple Coulomb scattering, which depends on the local heterogeneity of the phantom. Therefore, variance maps of the head phantom in coronal and sagittal views were varying greatly. Assuming that good image quality is required in the complete field-of-view, a fluence-modulated scan can reduce the imaging dose by 16.0% compared to a unit fluence scan, without any loss of diagnostic value. Equivalently, the signal-to-noise ratio could have been improved by 35% at equal dose.

For all phantoms and two different image variance targets, we could demonstrate considerable dose savings of 25.7% to 40.5% outside of the ROI. At the same time, the imaging dose inside the ROI increased compared to the unit fluence acquisition. Assuming that the ROI agrees with the treatment beam path and that treatment doses are several orders of magnitude higher than imaging doses, this increase is probably not relevant. At the same time, proton therapy allows for minimal doses outside the treatment beam path, requiring that this advantage is not compromised by frequent imaging. Mean imaging doses over the whole phantom were reduced for all combinations of phantoms and variance targets. Using a sensitometric phantom, we showed that RSP accuracy is not compromised by fluence modulation. RSP errors were comparable for modulated and un-modulated scans, and all below 1%, which is within the magnitude expected from literature.[12,19,35]

Imaging doses in fluence-modulated scans showed local increases and doses partially spilled out of the ROI. This may have impaired results in this study and could be caused by the fact that optimization was exclusively performed with a variance objective. Future studies should therefore include a dose objective outside of the ROI while keeping the variance objective inside the ROI, further developing ideas from studies for x-ray CT.[21] Moreover, the optimal choice of the contrast in the image variance prescription should be studied in the future, but is out of scope for this work.

Using a simple intersection-based approach also showed dose savings compared to unit fluence acquisitions. However, dose savings were considerably less compared to the optimized FMpCT scans and conformity of variance with the prescription was degraded. By construction, a prescription of constant variance is not possible with this approach.

Future work should also address the impact of iterative image reconstruction, which is frequently used for pCT imaging.[44–48] In contrast to the direct filtered backprojection algorithm used in this study, iterative reconstruction employs a regularization method (typically total variation), which reduces noise and whose optimal weight depends on the object and the fluence level.[49] While most fluence modulation studies for x-ray CT have been performed using filtered backprojection,[20,21] a first study[23] investigated a joint optimization of the fluence field and a spatially varying regularization parameter in the iterative reconstruction. For pCT, a comparison of iterative and direct reconstruction[47] showed comparable image quality. Preliminary work of the authors using an iterative reconstruction algorithm[46] and fluence modulation suggests feasibility of combining the two methods for pCT.

5. CONCLUSIONS

We developed a novel method for FMpCT using pencil beam scanning and demonstrated its feasibility in a simulation study. Dose reductions achieved by prescribing uniform variance were considerable, in particular for an anthropomorphic head phantom. This suggests the need for employing nonuniform fluence patterns in future pCT studies, whenever dose efficiency is a key requirement. Furthermore, the proposed method allows us to prescribe arbitrary image variance targets, which were shown to further reduce imaging dose outside of a given ROI. This can be of particular interest in the context of particle therapy and allow for daily imaging at a reduced imaging dose to healthy tissue outside of the treatment beam path.

ACKNOWLEDGMENTS

This work was supported by the German Research Foundation (DFG) project #388731804 “Fluence modulated proton computed tomography: a new approach for low-dose image guidance in particle therapy” and the DFG’s Cluster of Excellence Munich-Centre for Advanced Photonics (MAP), by the Bavaria-California Technology Center (BaCaTeC), and by the Franco-Bavarian university cooperation center (BayFrance).

CONFLICT OF INTEREST

The authors have no conflict to disclose.

*Senior authorship is shared equally.
[a)]Author to whom correspondence should be addressed. Electronic mail: guillaume.landry@med.uni-muenchen.de.

REFERENCES

1. Weber DC, Schneider R, Goitein G, et al. Spot scanning-based proton therapy for intracranial meningioma: long-term results from the Paul Scherrer institute. *Int J Radiat Oncol*. 2012;83:865–871.
2. Verma V, Lin SH, Simone CB, Mehta MP. Clinical outcomes and toxicities of proton radiotherapy for gastrointestinal neoplasms: a systematic review. *J Gastrointest Oncol*. 2016;7:644–664.
3. Nakajima K, Iwata H, Ogino H, et al. Clinical outcomes of image-guided proton therapy for stage I non-small cell lung cancer. *Int J Radiat Oncol*. 2017;99:E483–E484.
4. Kim H, Pyo H, Noh JM, et al. Preliminary result of definitive radiotherapy in patients with non-small cell lung cancer who have underlying idiopathic pulmonary fibrosis: comparison between X-ray and proton therapy. *Radiat Oncol*. 2019;14:19.
5. Landry G, Hua C-H. Current state and future applications of radiological image guidance for particle therapy. *Med Phys*. 2018;45:e1086–e1095.
6. Nenoff L, Matter M, Hedlund Lindmar J, Weber DC, Lomax AJ, Albertini F. Daily adaptive proton therapy – the key to innovative planning approaches for paranasal cancer treatments. *Acta Oncol*. 2019;58:1423–1428.
7. Hudobivnik N, Schwarz F, Johnson T, et al. Comparison of proton therapy treatment planning for head tumors with a pencil beam algorithm on dual and single energy CT images. *Med Phys*. 2016;43:495–504.

8. Wohlfahrt P, Möhler C, Stützer K, Greilich S, Richter C. Dual-energy CT based proton range prediction in head and pelvic tumor patients. *Radiother Oncol*. 2017;125:526–533.
9. Taasti VT, Bäumer C, Dahlgren CV, et al. Inter-centre variability of CT-based stopping-power prediction in particle therapy: survey-based evaluation. *Phys Imaging Radiat Oncol*. 2018;6:25–30.
10. Alaei P, Spezi E. Imaging dose from cone beam computed tomography in radiation therapy. *Phys Medica*. 2015;31:647–658.
11. Rinaldi I, Brons S, Gordon J, et al. Experimental characterization of a prototype detector system for carbon ion radiography and tomography. *Phys Med Biol*. 2013;58:413–427.
12. Schulte RW, Bashkirov V, Klock MC, et al. Density resolution of proton computed tomography. *Med Phys*. 2005;32:1035–1046.
13. Johnson RP, Bashkirov V, DeWitt L, et al. A fast experimental scanner for proton CT: technical performance and first experience with phantom scans. *IEEE Trans Nucl Sci*. 2016;63:52–60.
14. Esposito M, Waltham C, Taylor JT, et al. PRaVDA: the first solid-state system for proton computed tomography. *Phys Medica*. 2018;55:149–154.
15. Volz L, Piersimoni P, Bashkirov VA, et al. The impact of secondary fragments on the image quality of helium ion imaging. *Phys Med Biol*. 2018;63:195016.
16. Meyer S, Kamp F, Tessonnier T, et al. Dosimetric accuracy and radiobiological implications of ion computed tomography for proton therapy treatment planning. *Phys Med Biol*. 2019;64:1250008.
17. Yang M, Zhu XR, Park PC, et al. Comprehensive analysis of proton range uncertainties related to patient stopping-power-ratio estimation using the stoichiometric calibration. *Phys Med Biol*. 2012;57:4095–4115.
18. Hansen DC, Seco J, Sørensen TS, et al. A simulation study on proton computed tomography (CT) stopping power accuracy using dual energy CT scans as benchmark. *Acta Oncol*. 2015;54:1638–1642.
19. Dedes G, Dickmann J, Niepel K, et al. Experimental comparison of proton CT and dual energy x-ray CT for relative stopping power estimation in proton therapy. *Phys Med Biol*. 2019;64:165002.
20. Graham SA, Siewerdsen JH, Jaffray DA. Intensity-modulated fluence patterns for task-specific imaging in cone-beam CT. Proc. SPIE, **651003**; 2007.
21. Bartolac S, Graham S, Siewerdsen J, Jaffray D. Fluence field optimization for noise and dose objectives in CT. *Med Phys*. 2011;38:S2–S17.
22. Hsieh SS, Pelc NJ. Control algorithms for dynamic attenuators. *Med Phys*. 2014;41:061907.
23. Gang GJ, Mao A, Wang W, et al. Dynamic fluence field modulation in computed tomography using multiple aperture devices. *Phys Med Biol*. 2019;64:105024.
24. Wang W, Gang GJ, Siewerdsen JH, Stayman JW. Volume-of-interest imaging using multiple aperture devices. Proc. SPIE, **1094823**; 2019.
25. Bartolac S, Jaffray D. Compensator models for fluence field modulated computed tomography. *Med Phys*. 2013;40:121909.
26. Szczykutowicz TP, Mistretta CA. Experimental realization of fluence field modulated CT using digital beam attenuation. *Phys Med Biol*. 2014;59:1305–1326.
27. Szczykutowicz TP, Hermus J, Geurts M, Smilowitz J. Realization of fluence field modulated CT on a clinical TomoTherapy megavoltage CT system. *Phys Med Biol*. 2015;60:7245–7257.
28. Stayman JW, Mathews A, Zbijewski W, et al. Fluence-field modulated x-ray CT using multiple aperture devices. Proc. SPIE, **97830X**; 2016.
29. Huck SM, Fung GSK, Parodi K, Stierstorfer K. Technical Note: sheet based dynamic beam attenuator – a novel concept for dynamic fluence field modulation in x-ray CT. *Med Phys*. 2019;46:5528–5537.
30. Dedes G, De Angelis L, Rit S, et al. Application of fluence field modulation to proton computed tomography for proton therapy imaging. *Phys Med Biol*. 2017;62:6026–6043.
31. Dedes G, Johnson RP, Pankuch M, et al. Experimental fluence-modulated proton computed tomography by pencil beam scanning. *Med Phys*. 2018;45:3287–3296.
32. Lell MM, Kachelrieß M. Recent and upcoming technological developments in computed tomography. *Invest Radiol*. 2020;55:8–19.
33. Rädler M, Landry G, Rit S, Schulte RW, Parodi K, Dedes G. Two-dimensional noise reconstruction in proton computed tomography using distance-driven filtered back-projection of simulated projections. *Phys Med Biol*. 2018;63:215009.
34. Dickmann J, Wesp P, Rädler M, et al. Prediction of image noise contributions in proton computed tomography and comparison to measurements. *Phys Med Biol*. 2019;64:145016.
35. Giacometti V, Bashkirov VA, Piersimoni P, et al. Software platform for simulation of a prototype proton CT scanner. *Med Phys*. 2017;44:1002–1016.
36. Agostinelli S, Allison J, Amako K, et al. Geant4 - a simulation toolkit. *Nucl Instrum Methods Phys Res Sect A Accel Spectrom Detect Assoc Equip*. 2003;506:250–303.
37. Bashkirov VA, Schulte RW, Hurley RF, et al. Novel scintillation detector design and performance for proton radiography and computed tomography. *Med Phys*. 2016;43:664–674.
38. Schulte RW, Penfold SN, Tafas JT, Schubert KE. A maximum likelihood proton path formalism for application in proton computed tomography. *Med Phys*. 2008;35:4849–4856.
39. Rit S, Dedes G, Freud N, Sarrut D, Létang JM. Filtered backprojection proton CT reconstruction along most likely paths. *Med Phys*. 2013;40:031103.
40. Giacometti V, Guatelli S, Bazalova-Carter M, Rosenfeld A, Schulte R. Development of a high resolution voxelised head phantom for medical physics applications. *Phys Medica*. 2017;33:182–188.
41. Nelder JA, Mead R. A simplex method for function minimization. *Comput J*. 1965;7:308–313.
42. Wunderlich A, Noo F. Image covariance and lesion detectability in direct fan-beam x-ray computed tomography. *Phys Med Biol*. 2008;53:2471–2493.
43. Joseph PM. An improved algorithm for reprojecting rays through pixel images. *IEEE Trans Med Imaging*. 1982;1:192–196.
44. Penfold SN, Rosenfeld AB, Schulte RW, Schubert KE. A more accurate reconstruction system matrix for quantitative proton computed tomography. *Med Phys*. 2009;36:4511–4518.
45. Penfold SN, Schulte RW, Censor Y, Rosenfeld AB. Total variation superiorization schemes in proton computed tomography image reconstruction. *Med Phys*. 2010;37:5887–5895.
46. Hansen D, Bassler N, Sørensen T, Seco J. The image quality of ion computed tomography at clinical imaging dose levels. *Med Phys*. 2014;41:111908.
47. Hansen D, Sørensen T, Rit S. Fast reconstruction of low dose proton CT by sinogram interpolation. *Phys Med Biol*. 2016;61:5868–5882.
48. Schultze B, Censor Y, Karbasi P, Schubert KE, Schulte RW. An improved method of total variation superiorization applied to reconstruction in proton computed tomography. *IEEE Trans Med Imaging*. 2019;39:294–307.
49. Tian Z, Jia X, Yuan K, Pan T, Jiang SB. Low-dose CT reconstruction via edge-preserving total variation regularization. *Phys Med Biol*. 2011;56:5949–5967.